Chemistry Faculty Publications

Chemistry

10-4-2023

Modification of thermally activated delayed fluorescence emitters comprising acridan– pyrimidine moieties for efficient sky-blue to greenish-blue OLEDs

Yi-Zhen Li

Hsuan-Chi Liang

Chia-Hsun Chen

Ching-Huang Chiu

Bo-Yen Lin

See next page for additional authors

Recommended Citation

Li, Y.-Z., Liang, H.-C., Chen, C.-H., Chiu, C.-H., Lin, B.-Y., Tan, J. A., Lee, J.-H., Chiu, T.-L., & Leung, M. (2023). Modification of thermally activated delayed fluorescence emitters comprising acridan–pyrimidine moieties for efficient sky-blue to greenish-blue oleds. *Journal of Materials Chemistry C*, 11(41), 14395–14403. https://doi.org/10.1039/d3tc02820h

Authors

Yi-Zhen Li, Hsuan-Chi Liang, Chia-Hsun Chen, Ching-Huang Chiu, Bo-Yen Lin, Jake A. Tan, Jiun-Haw Lee, Tien-Lung Chiu, and Man-kit Leung

PAPER

Check for updates

Modification of thermally activated delayed fluorescence emitters comprising acridan–pyrimidine moieties for efficient sky-blue to greenish-blue OLEDs†

Yi-Zhen Li, [ID] [a] Hsuan-Chi Liang,[a] Chia-Hsun Chen, [ID] [b] Ching-Huang Chiu,[b] Bo-Yen Lin,*[c] Jake A. Tan, [ID] *[d] Jiun-Haw Lee, [ID] *[b] Tien-Lung Chiu [ID] *[e] and Man-kit Leung [ID] *[af]

Thermally activated delayed fluorescence (TADF) is a promising approach to harvest triplet excitons and achieve high-performance organic light-emitting diodes (OLEDs) for displays. In this study, we synthesized two new TADF emitters, **4Ac25CzPy** and **4Ac35CzPy**, featuring acridan–pyrimidine–carbazole moieties. Remarkably, a slight modification in the carbazole group position enables precise control of luminous color, resulting in emissions at 483 nm and 494 nm for **4Ac25CzPy** and **4Ac35CzPy**, respectively, in the electroluminescent device. Both compounds exhibit small energy difference between their singlet and triplet states (ΔE_{ST}) of 0.14 eV and 0.15 eV, confirming their TADF characteristics. Notably, OLEDs utilizing **4Ac35CzPy** achieve outstanding performance with the maximum external quantum efficiency (η_{EQE}) of 21.2% and a photoluminescence quantum yield of 65.1%. This high efficiency is attributed to efficient energy transfer from the host to the emitter. Moreover, the **4Ac35CzPy** device exhibits a high light out-coupling efficiency of 0.3, further enhancing its remarkable performance.

Introduction

Thermally activated delayed fluorescence (TADF) materials are promising metal-free organic light emitting compounds for display and lighting applications. Emitters with TADF properties can harvest both singlet and triplet excitons in organic light emitting diodes (OLED) to achieve 100% of exciton utilization efficiency and internal quantum efficiency (IQE).[1–4] The TADF molecules usually contain strong donors and acceptors that are orthogonally linked by aromatic rings.[5] This design facilitates

[a] *Department of Chemistry, National Taiwan University, Taipei 10617, Taiwan. E-mail: mkleung@ntu.edu.tw*

[b] *Graduate Institute of Photonics and Optoelectronics and Department of Electrical Engineering, National Taiwan University, Taipei 10617, Taiwan. E-mail: jiunhawlee@ntu.edu.tw*

[c] *Department of Opto-Electronic Engineering, National Dong Hwa University, Hualien 974301, Taiwan. E-mail: boyenlin@gms.ndhu.edu.tw*

[d] *Department of Chemistry, Gottwald Center for the Sciences, University of Richmond, Richmond, Virginia 23173, USA. E-mail: jake.tan@richmond.edu*

[e] *Department of Electrical Engineering, Yuan Ze University, Taoyuan 32003, Taiwan. E-mail: tlchiu@saturn.yzu.edu.tw*

[f] *Advanced Research Center for Green Materials Science and Technology, National Taiwan University, No. 1, Sec. 4, Roosevelt Rd, Taipei 10617, Taiwan*

† Electronic supplementary information (ESI) available. CCDC 2285137 and 2285159. For ESI and crystallographic data in CIF or other electronic format see DOI: https://doi.org/10.1039/d3tc02820h

the material to possess a small singlet–triplet energy splitting (ΔE_{ST}), which benefits the reverse intersystem crossing (rISC) and boosts the OLED efficiency.[6,7] In addition, the orthogonally linked aromatic moieties can act as steric shields, preventing the molecules from π-stacking, and suppressing the intermolecular exciton quenching effects.

Recently, acridan moiety has found a special place in TADF.[8–10] For example, 9,9-dimethyl-9,10-dihydroacridine, shows a moderately strong electron-donating ability and high-energy triplet states that is a suitable candidate on the design of TADF materials. Pyrimidine, on the other hand, is a promising electron acceptor that shows excellent performance in TADF. Emitters derivatized at the 2, 4, 5 and 6 positions of pyrimidine have been explored.[11–13]

Yasuda reported a series of D–A type pyrimidine-based TADF materials with a donor linked at the 2-position (Fig. 1), among which **Ac-PM** is the bluest emitter in the series with the

Fig. 1 Molecular structures of pyrimidine derivatives.

This journal is © The Royal Society of Chemistry 2023

J. Mater. Chem. C, 2023, **11**, 14395–14403 | **14395**

maximum device external quantum efficiency (η_{EQE}) value of 11.4%.[14] Increasing the steric shields by introducing bulky phenyl substituents and rigid spiro-ring can enhance the η_{EQE} to 15.5% for **Ac-46DPPM** and to 20.4% for **MFAc-PPM** with the electroluminescence λ_{max} slightly red-shifted to 464 nm and 470 nm, respectively.[15] Other than the D–A type **Ac-PM series**, pyrimidine based TADF emitters with twisted D–A–D architecture allow to feature substantially efficient quantum efficiency exceeding 90% and with a high η_{EQE} of 20.8%.[16]

On the other hand, when an electron-withdrawing cyano group (**Pm5**) is introduced at the 5-position of the pyrimidine ring, the η_{EQE} increases to 30.6%. However, the λ_{max} is significantly red-shifted to 541 nm.[17] Therefore, improving the η_{EQE} value and at the same time retaining the blue spectral emission is still a challenging problem to investigate.

In the present work, we put our efforts on developing new D–A type pyrimidine-based emitters, and improving their electroluminescence (EL) performance. We adopt acridan–pyrimidine (**Ac-PM**) as a basic framework and incorporate carbazole functionalities onto the **Ac-PM** skeleton. Consequently, two novel TADF materials of **4Ac25CzPy** and **4Ac35CzPy** are derived as shown in Fig. 2. Instead of having a similar D–A type design, additional carbazole moieties are substituted at different positions of central phenyl linker to disperse the HOMO delocalization. The carbazolyl groups at different substituted positions bring dissimilar impact on their spectral and electronic properties. Indeed, we will report in latter sections that the fluorescent spectrum of **4Ac25CzPy** shows a hypsochromic shift emission by approximately 15 nm than that of **4Ac35CzPy**. The unsymmetrical orientation of carbazole moieties of **4Ac25CzPy** leads acridan and pyrimidine a larger torsional angle to the central phenyl linker, when comparison with **4Ac35CzPy**. Since the substituents are more or less perpendicular to central phenyl, the strong internal charge transfer (ICT) through π-conjugation is largely disrupted. A higher lying singlet–triplet energy level could be maintained to show blue emission. Intriguingly, both compounds have a similar ΔE_{ST} (<0.2 eV) that are satisfied to be TADF materials with similar quantum yields of around 70%.

Notedly the molecule packing of these materials in their solid states and their EL spectra are quite different. OLEDs utilizing **4Ac25CzPy** and **4Ac35CzPy** show an EL emission peaked at 484 and 492 nm, whose optimized efficiency performance can reach the highest η_{EQE} of 12.4% and 21.2%, respectively. Although the η_{EQE} of the device could not achieve an ideal value of 25%, the maximum η_{EQE} of **4Ac35CzPy** is comparable to other reported pyrimidine-based materials.[18–20] Further studies reveal
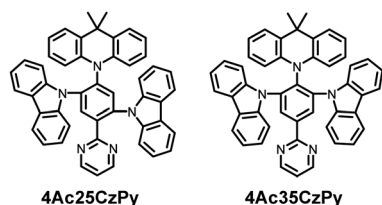
that **4Ac35CzPy** device exhibits a higher light outcoupling efficiency and device efficiency as well.[21]
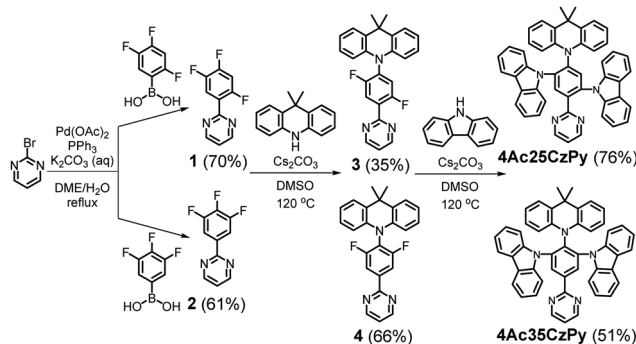
Results and discussion

Synthesis of 4Ac25CzPy and 4Ac35CzPy

The synthetic routes for **4Ac25CzPy** and **4Ac35CzPy** are illustrated in Scheme 1 and ESI.† Both targets were synthesized from the corresponding trifluorophenylboronic acid with 2-bromo-pyrimidine *via* Suzuki–Miyaura cross-coupling reactions. Subsequently, intermediates **1** and **2** were reacted with 9,9-dimethyl-9,10-dihydroacridine (Ac), followed by 2 equivalents of carbazole through nucleophilic aromatic substitution (S_NAr) to afford **4Ac25CzPy** and **4Ac35CzPy** respectively. Since the 4-fluoro substituent on **1** and **2** is relatively reactive, the acridan group could therefore be introduced selectively to the 4-position in the first S_NAr step. **4Ac25CzPy** and **4Ac35CzPy** were purified by sublimation under reduced pressure (1×10^{-5} torr) and identified by ^{1}H NMR spectroscopy, ^{13}C NMR spectroscopy, high-resolution mass spectrometry (HRMS) and single-crystal X-ray diffraction (XRD). The synthetic method and corresponding NMR spectra of **4Ac25CzPy** and **4Ac35CzPy** are presented in Fig. S1–S16 (ESI†). In addition to HRMS and NMR identification, we conducted high-performance liquid chromatography (HPLC) and elemental analysis (EA) to assess their purity, as shown in Fig. S17 and S18 (ESI†).

Crystallographic analysis

X-ray crystallographic analysis of **Ac25CzPy** suggests that the acridan and the carbazole units are more or less perpendicular to the central benzene ring (Fig. 3). The dihedral angle between the central benzene ring and acridan moiety is 83.51° (59.05°). The acridan moiety is non-planar and bends away from the adjacent carbazole unit so as to avoid the steric repulsion in between. On the other hand, the dihedral angle between the benzene and the pyrimidine is 41.76°.

Perhaps due to the symmetrical 1,2,3-*ortho*-substituent arrangement, the middle acridan may experience the same repulsions from carbazoles on both sides. Therefore, the acridan moiety in **4Ac35CzPy** is more planar in comparison with that in **Ac25CzPy**. The acridan and carbazole units are tilted towards the same direction so that a dihedral angle of 69.95° (65.39°)

Fig. 2 Molecular structures of **4Ac25CzPy** and **4Ac35CzPy**.

Scheme 1 Synthetic routes and molecular structures of **4Ac25CzPy** and **4Ac35CzPy**.

14396 | *J. Mater. Chem. C*, 2023, **11**, 14395–14403

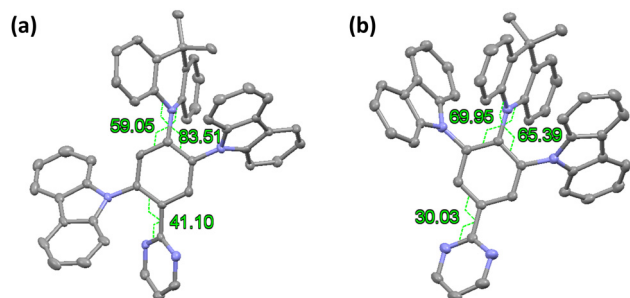This journal is © The Royal Society of Chemistry 2023

Fig. 3 Molecular structures of (a) **4Ac25CzPy** and (b) **4Ac35CzPy** with thermal ellipsoids drawn at a 50% probability level.

between the acridan and the central benzene is observed, and hence partial π-conjugations are facilitated. In addition, in the absence of the *ortho*-carbazole unit, the pyrimidine shows a smaller dihedral angle of 30.03°, which is smaller than that of **4Ac25CzPy**. All these allow a better π-conjugation between the acridan or the pyrimidine units in **4Ac35CzPy**, leading to a smaller HOMO–LUMO gap and therefore red-shifted of the emission to greenish-blue.

Density functional theory (DFT) calculations

To justify our design strategy on these materials for TADF applications and to investigate the interaction between donor and acceptor, we performed density functional theory (DFT) calculations to obtain the frontier molecular orbitals and energy levels of **4Ac25CzPy** and **4Ac35CzPy**. The Becke 3-parameter Lee–Yang–Parr (B3LYP)[22–25] hybrid functional was used together with the def2-TZVP(-f) basis set. The RIJCOSX approximation[26] with def2/J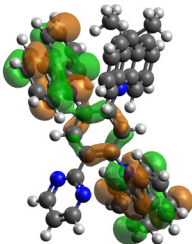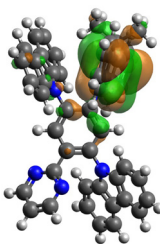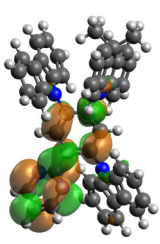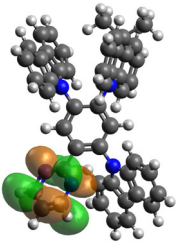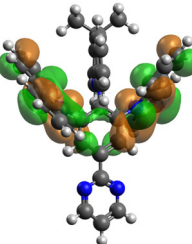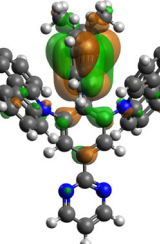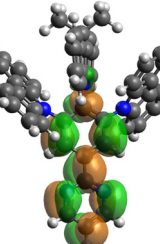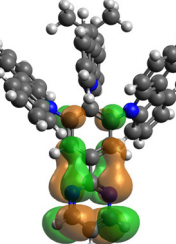 and def2-TZVP/C as auxiliary basis sets were used to speed up the DFT calculation. Dispersion interactions were accounted for using Grimme's D3 dispersion correction with Becke–Johnson damping (D3BJ).[27] To account for the environment effects, conductor-like polarizable continuum model (CPCM)[28] calculations were performed with 2-MeTHF ($\varepsilon = 6.97$) as solvent. All electronic structure calculations were performed using the ORCA 5.0.3 suite of programs.[29–31]

The structures for **4Ac25CzPy** and **4Ac35CzPy** were optimized at their respective S_0 potential energy surfaces (PESs). Frequency calculations were then performed to confirm that the obtained structures correspond to a minimum at their respective PES. To aid in understanding the nature of the excited S_1 and T_1 states, we first examined the molecular orbitals of **4Ac25CzPy** and **4Ac35CzPy**.

Table 1 shows the B3LYP-D3BJ/def2-TZVP(-f)/CPCM(2-MeTHF) molecular orbitals: HOMO−1, HOMO, LUMO, and LUMO+1 as well as their energies, in units of electron volt (eV), for **4Ac25CzPy** and **4Ac35CzPy** at their S_0 minimum structures. Both of their HOMOs are localized on the acridan fragment, while their HOMO−1 are delocalized on carbazole–benzene–carbazole fragment. As for the LUMO and LUMO+1, both correspond to a π-molecular orbital that is delocalized on the benzene–pyrimidine fragment, except for the LUMO+1 of **4Ac25CzPy**, which is mainly localized on the pyrimidine fragment. Both materials have small HOMO and LUMO overlap, it is consistent with the photophysical TADF results that achieve a high quantum yield.

To understand the role of these molecular orbitals on the excited states, TD-DFT calculations with the Tamm–Dancoff approximation (TDA) were performed at the B3LYP-D3BJ/def2-TZVP(-f)/CPCM(2-MeTHF) level to calculate the S_1 and T_1 vertical excitation energies at the ground state geometry. In **4Ac25CzPy**,

Table 1 B3LYP-D3BJ/def2-TZVP(-f)/CPCM(2-MeTHF) orbitals and their corresponding orbital energies (in eV) for **4Ac25CzPy** and **4Ac35CzPy** at their respective minimum S_0 structures

Species	HOMO−1	HOMO	LUMO	LUMO+1
4Ac25CzPy	−5.64 eV	−5.23 eV	−1.80 eV	−1.46 eV
4Ac35CzPy	−5.72 eV	−5.23 eV	−1.97 eV	−1.53 eV

This journal is © The Royal Society of Chemistry 2023

J. Mater. Chem. C, 2023, **11**, 14395–14403 | **14397**

the S_0 to S_1 vertical excitation energy is 2.853 eV, while the S_0 to T_1 vertical excitation energy is 2.782 eV. Meanwhile, in **4Ac35CzPy**, the S_0 to S_1 vertical excitation energy is 2.731 eV, while the S_0 to T_1 vertical excitation energy is 2.561 eV. In both species the S_1 and T_1 excited states correspond to a HOMO to LUMO excitation. The square of the wave-function coefficients for the HOMO to LUMO transitions are greater than 94%. Vertical excitation energies for higher excited states are provided in Table S1 (ESI†).

The capability of **4Ac25CzPy** and **4Ac35CzPy** to exhibit TADF characteristic is based on the rate of rISC. Since TADF contains a rISC process that involves a population transfer from the T_1 state back to the S_1 state. Excited state geometry optimizations were performed for **4Ac25CzPy** and **4Ac35CzPy** at these excited states. These geometry optimizations were conducted using TDA-B3LYP-D3BJ/def2-TZVP(-f)/CPCM(2-MeTHF) method. Table S2 (ESI†) shows the corresponding adiabatic excitation energies (ΔE_{ST}^{Adia}) for these species. As shown in Table S2 (ESI†), the ΔE_{ST}^{Adia} for **4Ac25CzPy** is 0.038 eV, while for **4Ac35CzPy** the ΔE_{ST}^{Adia} is 0.088 eV. Such a small ΔE_{ST}^{Adia} do suggest that rISC can be thermally activated. Hence, based on their small singlet–triplet gap, both **4Ac25CzPy** and **4Ac35CzPy** can exhibit TADF.

A natural transition orbital (NTO) analysis on the respective minimum geometries of the S_1 and T_1 states for **4Ac25CzPy** and **4Ac35CzPy** reveals that the NTOs corresponding to the hole and electron have a small orbital overlap, which is an indication of a strong charge transfer character for these excited states (Table S3, ESI†). To characterize the nature of these S_1 and T_1 states further, Inter-Fragment Charge Transfer (IFCT) calculations were performed using the multifunctional wavefunction analyzer (Multiwfn)[32] package. Table 2 shows the apparent percent charge transfer (CT) and percent local excitation (LE) for **4Ac25CzPy** and **4Ac35CzPy**. We note that both S_1 and T_1 states for these species have a dominant CT character, which agrees with the NTO picture. Also, since the S_1 and T_1 states for **4Ac25CzPy** have a stronger CT character when compare with those for **4Ac35CzPy**, the ΔE_{ST}^{Adia} for **4Ac25CzPy** is then expected to be smaller in comparison with **4Ac35CzPy**. We recall that the calculated ΔE_{ST}^{Adia} for **4Ac25CzPy** is 0.038 eV, while that for **4Ac35CzPy** is 0.088 eV. Notably, significant CT contribution of the T_1 state would effectively reduce the ΔE_{ST} value. In our theoretical calculation, we expect that **4Ac25CzPy** and **4Ac35CzPy** would definitely have considerable potential to become excellent TADF materials.[33]

In addition to the ΔE_{ST}^{Adia}, other key quantities that determine the rate of rISC are the spin–orbit coupling between the S_1 and T_1 state,[34,35] and the reorganization energy (λ). The magnitude of S_1 and T_1 spin–orbit coupling matrix element (SOCME) for **4Ac25CzPy** and **4Ac35CzPy** were calculated at the

T_1 state's minimum geometry and reorganization energy are provided in Table S2 (ESI†). The $|T_1|\hat{H}_{SO}|S_1|$ for **4Ac25CzPy** and **4Ac35CzPy** in 2-MeTHF are within the same order of magnitude. In particular, 0.224 cm^{-1} for **4Ac25CzPy** and 0.210 cm^{-1} for **4Ac35CzPy**.

Thermal properties

The thermal properties of **4Ac25CzPy** and **4Ac35CzPy** were evaluated by thermogravimetric analysis (TGA) and differential scanning calorimetry (DSC), and the results and the data are provided in Fig. S19 and S20 (ESI†), respectively. **4Ac25CzPy** and **4Ac35CzPy** both exhibit a high thermal decomposition temperature (T_d, corresponding to 5% weight loss) of 378 and 344 °C, respectively. Thus, **4Ac25CzPy** is structurally more robust than **4Ac35CzPy**. We tentatively attribute to the highly congested 1,2,3-*ortho*-substituent arrangement of the electron-rich acridan and carbazole units that may cause electronic repulsion between the substituents.

In the DSC analysis for **4Ac35CzPy**, the glass transition temperature (T_g), crystallization temperature (T_c) or melting temperature (T_m) could not be observed below 350 °C. For **4Ac25CzPy**, high T_g and T_m values are measured at 146 and 306 °C, respectively. Besides, T_g and T_m, a T_c could be observed at 243 °C in the second round of DSC scanning. In short, **4Ac25CzPy** and **4Ac35CzPy** show high thermal stability that may be beneficial to the operational lifetime of their OLEDs.

Electrochemical properties

The energy levels for **4Ac25CzPy** and **4Ac35CzPy** were evaluated by cyclic voltammetry (CV) and differential pulse voltammetry (DPV), the corresponding electrochemical properties are summarized in Table 3 and Fig. S21 (ESI†). The oxidation scan was measured in dichloromethane, and the reductive scan was performed in *N*,*N*-dimethylformamide. The HOMO and LUMO levels were calculated by the DPV value of the oxidation and the reduction. The values of E_{DPV}^{ox} and E_{DPV}^{re} for **4Ac25CzPy** and **4Ac35CzPy** are 0.59/−2.20 and 0.56/−2.11 V, when using ferrocene as the internal standard. Therefore, the HOMO/LUMO levels of 5.51/2.78 eV and 5.47/2.85 eV for **4Ac25CzPy** and **4Ac35CzPy** are estimated respectively. The higher HOMO with a lower LUMO levels for **4Ac35CzPy** implies that **4Ac35CzPy** should have a stronger electron donor and a better electron acceptor characteristic. These are consistent with our previous results in the X-ray crystallographic analysis as well as in our theoretical studies.

Photophysical properties

The photophysical properties including UV-vis absorption and low temperature photoluminescence spectra of **4Ac25CzPy** and **4Ac35CzPy** are shown in Fig. 4(a) and (b), and key parameters are summarized in Table 3. UV-vis absorption was measured in THF solution, low temperature fluorescence (LTFL) and low temperature phosphorescence (LTPh) were measured in 2-methyltetrahydrofuran (2-MeTHF) with a concentration of 1×10^{-5} M at 77 K. 2-MeTHF has been used for measurement in order to avoid crystallization of the solvent at low temperature.

Table 2 Apparent charge transfer (CT) and local excitation (LE) percentage characters for the S_1 and T_1 excited states with 2-MeTHF as solvent

Molecule	S_1 state		T_1 state	
	CT (%)	LE (%)	CT (%)	LE (%)
4Ac25CzPy	90.4	9.6	86.5	13.5
4Ac35CzPy	84.0	16.0	78.3	21.7

14398 | *J. Mater. Chem. C*, 2023, **11**, 14395–14403

This journal is © The Royal Society of Chemistry 2023

Table 3 Photophysical properties for **4Ac25CzPy** and **4Ac35CzPy**

Material	Absorption [nm] solution[a]/film		Emission [nm] solution/film							Energy level[f] [eV]
	λ_{onset}^{abs}	E_g^b [eV] solution/film	$\lambda_{max}^{FL\ a}$	$\lambda_{onset}^{LTFL\ c}$	$\lambda_{onset}^{LTPH\ c}$	S_1^d [eV]	T_1^d [eV]	ΔE_{ST} [eV]	Φ^e [%]	HOMO/LUMO
4Ac25CzPy	399/436	3.1/2.8	508/493	378	419	3.28	2.96	0.15	70	5.7/2.9
4Ac35CzPy	436/460	2.8/2.7	480/508	423	456	2.93	2.72	0.14	70	5.6/2.9

[a] Measure in solution of THF (1×10^{-5} M). [b] Estimation of energy gap by the equation of $1240.8/\lambda_{onset}^{abs}$. [c] Measured in 2-MeTHF with the concentration of $\times 10^{-5}$ M at 77 K. [d] Estimation of singlet and triplet state energy is using equation of $1240.8/\lambda_{onset}^{LTFL}$ and $1240.8/\lambda_{onset}^{LTPH}$. [e] Phenanthrene was used as a reference in the cyclohexane. [f] Value in film: HOMO is measured by AC-II and LUMO = HOMO − E_g.

Furthermore, the thin film photoluminescence (PL), which is presented in Fig. 4(c), was also measured to simulate the emission in the device.

As shown in Fig. 4(a) and (b), **4Ac25CzPy** and **4Ac35CzPy** exhibit similar UV absorption profiles, in which the strong absorption at peaked at 290 nm is assigned to the π–π* transitions of conjugated aromatic moieties. The weaker absorption between 300–350 nm usually arises from the carbazole n–π* transition, and the weakest absorption between 350–450 nm is due to the intramolecular charge transfer (ICT) transitions mainly from the acridan to the pyrimidine unit. However, as we mentioned before, due to the stronger acridan–phenylene–pyrimidine π-conjugation in **4Ac35CzPy**, the ICT absorption at around 400 nm is significantly stronger than that of **4Ac25CzPy**. The onset of absorption for **4Ac25CzPy** and **4Ac35CzPy** in solution are 399 and 436 nm, respectively and were estimated from the spectral data that corresponds to optical energy gap (E_g) of 3.1 and 2.8 eV, respectively.

Fluorescence emissions for **4Ac25CzPy** and **4Ac35CzPy** in THF at room temperature are red shifted significantly. The room temperature FL spectra for **4Ac25CzPy** and **4Ac35CzPy** show an emission maximum at 508 and 480 nm, respectively. Their corresponding luminous colour exhibit greenish-blue (**4Ac25CzPy**) and bluish-green (**4Ac35CzPy**), respectively. These results indicate that the spectral properties of **4Ac25CzPy** and

4Ac35CzPy can be significantly perturbed by the environment. This is perhaps originated from the ICT character of the TADF emitters. Fig. 5(a) and (b) show the solvatochromism of **4Ac25CzPy** and **4Ac35CzPy** in solvents with various polarities. The emission maximum of **4Ac25CzPy** spans a range of about 100 nm in various solvents, from 456 nm in cyclohexane red-shifting to 552 nm in acetonitrile. Similarly, the emission maximum of **4Ac35CzPy** spans a range of about 90 nm, from 462 nm in cyclohexane red-shifting to 548 nm in acetonitrile. These results are consistent with the assumption of the ICT character in their S_1 states; polar solvents can stabilize their polar S_1 excited state and hence leading to a red-shift of their emissions.

The triplet states energy for **4Ac25CzPy** and **4Ac35CzPy** were determined from the onset of their LTPh spectra, in which the energy of 2.96 and 2.72 eV for their T_1 states have been found respectively. The energy splitting of 0.15 and 0.14 eV of their S_1 and T_1 states (ΔE_{ST}) are therefore estimated; both are lower than 0.2 eV, implying their potential for harvesting triplet excitons through rISC process for TADF emissions. In solid thin film, their fluorescence emissions peaked at 493 nm and 508 nm for **4Ac25CzPy** and **4Ac35CzPy**. These peaks are red-shifted when compared to measurements in cyclohexane (Fig. 4(c) and Table 3). We tentatively attribute the bathochromic shifts in the solid state to the intermolecular π-stacking effects of the molecules. Nevertheless, the photoluminescence of **4Ac25CzPy** and **4Ac35CzPy** can still be considered as sky-blue to bluish green.

4Ac25CzPy and **4Ac35CzPy** in doped films, using o-DiCbzBz[36] as host with volume concentration of 12%, show an unexpectedly high photoluminescence quantum yield (PLQY) values of 52.8% and 65.1% (Fig. S22, ESI† and Table 4). Since the ΔE_{ST} of **4Ac25CzPy** and **4Ac35CzPy** are smaller than 0.2 eV, we wonder if
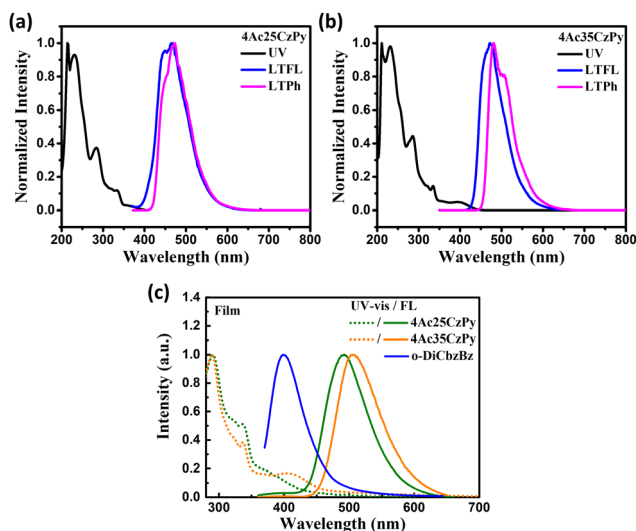

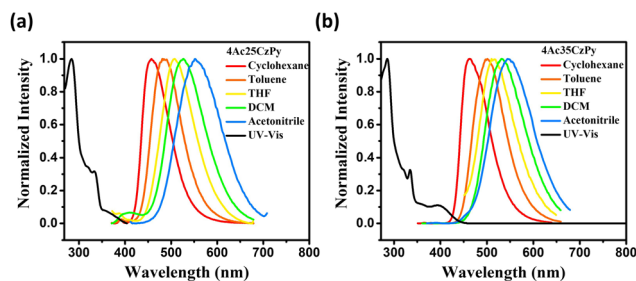**Fig. 4** UV-vis and PL spectra of (a) **4Ac25CzPy** and (b) **4Ac35CzPy** in solution; (c) thin film.

Fig. 5 Solvatochromism of (a) **4Ac25CzPy** and (b) **4Ac35CzPy**.

Table 4 Physical data of **4Ac25CzPy** and **4Ac35CzPy**-doped film

Material	$\Phi_{\text{total}}/\Phi_{\text{prompt}}/\Phi_{\text{delay}}{}^{a}$ [%]	$\tau_{\text{p}}{}^{b}$ [ns]	$\tau_{\text{d}}{}^{b}$ [μs]	$k_{\text{r,s}}{}^{c}$ [× 10^7 S^{-1}]	$k_{\text{nr,T}}{}^{c}$ [× 10^3 S^{-1}]	$k_{\text{ISC}}{}^{d}$ [× 10^7 S^{-1}]	$k_{\text{rISC}}{}^{d}$ [× 10^4 S^{-1}]
4Ac25CzPy	52.8/11.4/41.4	8.2	60.0	1.4	8.9	10.9	6.8
4Ac35CzPy	65.1/11.7/53.4	11.8	73.2	1.0	5.4	7.4	7.0

[a] Photoluminescence quantum yield of overall, prompt and delayed fluorescence. [b] Exciton lifetime of prompt and delayed fluorescence obtained from TrPL. [c] Rate constant of radiative decay from S_1 to S_0 ($K_{\text{r,s}}$) and nonradiative decay of T_1 to S_0 ($K_{\text{nr,T}}$). [d] Rate constant of intersystem crossing (ISC) and reverse intersystem crossing (rISC).

TADF does play important roles in the light emission process. To verify this hypothesis, transient PL (TrPL) measurements are conducted (Fig. 6), where both compounds show a typical TADF behaviour with a nanosecond-scale prompt component followed by a microsecond-scale delayed component. The prompt exciton lifetime (τ_{p}) and delayed exciton lifetime (τ_{d}) are monitored by fitting the luminescence decay curves according to the unimolecular exponential decay model. The $\tau_{\text{p}}/\tau_{\text{d}}$ of 8.15 ns/60 μs and 11.8 ns/73.2 μs for **4Ac25CzPy** and **4Ac35CzPy** are therefore estimated, respectively (Table 4). The quantum efficiency of the prompt and delay fluorescence can then be obtained as well, which was measured from the intensity ratio by counting the TrPL signals from 0 to 5 μs as prompt component and the remaining as TADF component. Thus, the total PLQY values (Φ_{total}) of **4Ac25CzPy** and **4Ac35CzPy** can be separated into the prompt (Φ_{prompt}) and the delayed (Φ_{delayed}) fluorescence emissions. The rate constants of k_{r}, k_{nr}, k_{ISC}, k_{rISC} for thin films have been also evaluated and summarized (Table 4) according to the reported method,[37,38] and the details regarding calculation can be accessed in the ESI† as well. Notably, **4Ac35CzPy** exhibits a faster rate constant of rISC of 7.0×10^4 s^{-1} relative to **4Ac25CzPy** of 6.8×10^4 s^{-1}, which might benefit better device performance in OLEDs.

Electroluminescence

According to the above evaluations, we wonder if **4Ac25CzPy** and **4Ac35CzPy** can be used as blue light TADF emitters for OLEDs. The devices with a configuration of ITO/1,1-bis[(di-4-tolylamino) phenyl] cyclohexane, TAPC/N,N-dicarbazolyl-3,5-benzene, mCP/emitting layer (EML)/diphenylbis[4-(pyridin-3-yl)phenyl]silane, DPPS/LiF/Al is fabricated and used in our tests. **4Ac25CzPy** and **4Ac35CzPy** were doped respectively into o-DiCbzBz[36] to form the EML. TAPC, mCP, and DPPS, as shown in Fig. 7, are used correspondingly as the hole transporting layer (HTL), electron blocking layer (EBL) and electron transporting layer (ETL). The HOMO and LUMO values of the materials shown in the energy level alignment diagram in Fig. 7 come from the literature.[39] The HOMO of **4Ac25CzPy** and **4Ac35CzPy** are determined by AC-II (Fig. S23, ESI†), whose LUMO are calculated from the HOMO and the optical gap E_{g}.

The OLED devices with **4Ac35CzPy** and **4Ac25CzPy** as the emitters were optimized through a sequence of optimization procedure including variation of dopant concentration, DPPS thickness and EML thickness (Tables S4, S5 and Fig. S24–S26, ESI†). Consequently, the optimal device structure for the **4Ac35CzPy** OLED is ITO/TAPC (50 nm)/mCP (10 nm)/12% **4Ac35CzPy**: o-DiCbzBz (30 nm)/DPPS (55 nm)/LiF (0.8 nm)/Al (120 nm) and the devices of **4Ac25CzPy** were then fabricated by using the same device structure for comparison.

EL performance of the **4Ac25CzPy** and **4Ac35CzPy** devices including spectral behaviour, current density–luminance–voltage (J–L–V) characteristics and efficiency curves are summarized in Fig. 8 and Table 5. Fig. 8(a) shows the EL emissive spectra peaked at 483 and 494 nm for **4Ac25CzPy** and **4Ac35CzPy**, corresponding to Commission internationale de l'éclairage (CIE) 1931 coordinates of (0.156, 0.396) and (0.185, 0.403). The OLED devices of **4Ac25CzPy** and **4Ac35CzPy** have a turn-on voltage (V_{on}) of 2.9 and 3.4 V at 1 cd m^{-2} and achieve the highest luminance of 2635 and 3288 cd m^{-2} (Fig. 8(b)). The OLED of **4Ac25CzPy** shows the highest current efficiency (η_{c}) of 31.48 cd A^{-1}, power efficiency (η_{p}) of 28.3 lm W^{-1}, and η_{EQE} of 12.4%, respectively. By contrast, **4Ac35CzPy** device shows the highest current efficiency (η_{c}) of 53.3 cd A^{-1}, η_{p} of 48.1 lm W^{-1}, and η_{EQE} of 21.2%. In addition, these devices still demonstrate reasonable efficiency at high luminance of 1000 cd m^{-2} with η_{EQE} of 6.6% and 11.9% for **4Ac25CzPy** and **4Ac35CzPy** devices, out of which the efficiency roll-off is essentially from TTA, triplet-polaron annihilation (TPA) and/or the loss of carrier balance in OLEDs.[40] Other than the above reasons, another contributing factor might be the long triplet life-times that are reflected on their significantly long
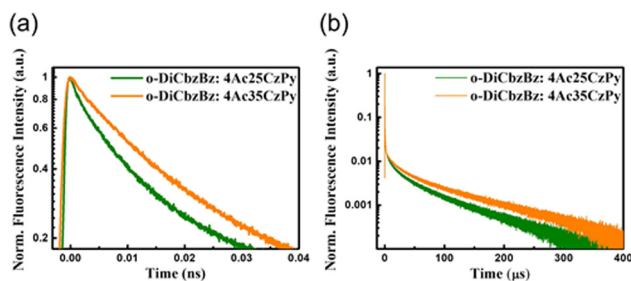

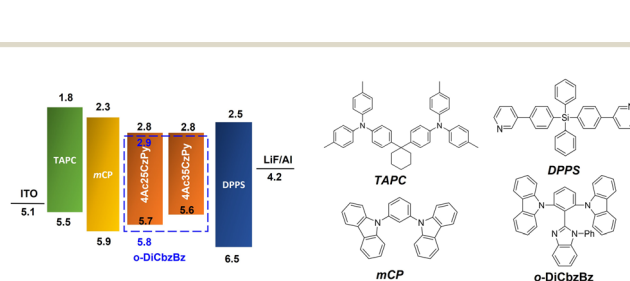**Fig. 6** TrPL of (a) prompt and (b) delayed decay curves for **4Ac25CzPy** and **4Ac35CzPy** in doped film.

Fig. 7 Energy band diagram and chemical structure of materials used in OLEDs.
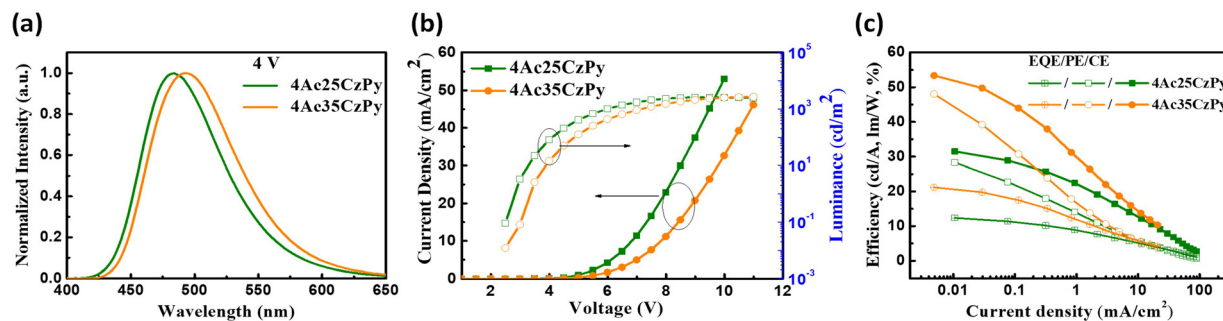
Fig. 8 (a) EL spectrum at 4 V; (b) $J-L-V$ characteristics; (c) the plot of efficiency *versus* current density for **4Ac25CzPy** and **4Ac35CzPy** devices.

Table 5 EL performance for **4Ac25CzPy** and **4Ac35CzPy** devices

Device	$V_{on}{}^a$ (V)	L^b (cd m⁻²)	$\eta_{CE}{}^c$ (cd A⁻¹)	$\eta_{PE}{}^c$ (lm W⁻¹)	$\eta_{EQE}{}^c$ (%)	λ_{EL} (nm)	CIE^d (x, y)
4Ac25CzPy	2.9	2635	31.5/27.6/16.6	28.3/20.7/8.7	12.4/10.9/6.6	483	(0.156, 0.396)
4Ac35CzPy	3.4	2724	53.3/44.9/31.1	48.1/32.9/14.9	21.2/17.2/11.9	494	(0.185, 0.403)

^{a} Turn on voltage at 1 cd m⁻². ^{b} Maximum luminance. ^{c} Measured at maximum, 100 cd m⁻², 1000 cd m⁻². ^{d} Measure at 4 V.

luminescence decay times. This would lead to an accumulation of excessive triplet excitons at higher applied voltages, leading to issues associated with triplet–triplet quenching and subsequent efficiency reduction. In particular, characterized by its more prolonged fluorescence delay, **4Ac35CzPy** experiences a more obvious reduction in efficiency.

The TADF behaviours of the triplet excitons in EL device have been further investigated by using transient electroluminescence (TrEL) measurements (Fig. 9). The TrEL of the OLED are monitored under various driven current density. The TrEL of **4Ac25CzPy** and **4Ac35CzPy** devices show typical TADF decay behaviour under all driving conditions. The long EL decay attributed to the triplet excitons could last several hundred microseconds.[41] Due to the triplet-polaron annihilation, the decay time decreases while the driven voltage pulse increases, which are reflected on the current density decay. All these observations in TrEL are consistent with the hypothesis of exciton harvesting through TADF (Fig. 6).

Although the PLQY values of around 70% for both **4Ac25CzPy** and **4Ac35CzPy** are similar in solution, the PLQY values are different in their doped films in *o*-DiCbzBz, with **4Ac35CzPy** exhibiting higher PLQY value (65%) compared to that of **4Ac25CzPy** (53%) (Table 3). This disparity may still have a contribution to the

EL performance so that **4Ac35CzPy** achieves a higher η_{EQE} than **4Ac25CzPy**. In general, the PLQY in solid state is typically lower than that in solution state due to the concentration quenching effect. To prevent that, host-dopant system is commonly employed, and therefore energy transfer efficiency of host-dopant system is a vital factor for reaching high efficiency OLEDs.

To investigate the energy transfer efficiency in OLEDs, the UV-vis spectra of dopants and FL spectrum of *o*-DiCbzBz, the host, were measured and are shown in Fig. 4(b). The good spectral overlap between the UV-vis of **4Ac25CzPy** and **4Ac35CzPy** and FL of *o*-DiCbzBz should allow efficient Förster energy transfer in these system.[42] Due to the presence of the large CT absorption band at around 400 nm, one may expect that the energy transfer from *o*-DiCbzBz to **4Ac35CzPy** will be more effective. This may account for its high PLQY value of 65.1% in solid state. Notably, the value of **4Ac35CzPy** is comparable to that in solution state (70%), indicating efficient energy transfer. In contrast, a significant difference in PLQY between solution and solid states is observed for **4Ac25CzPy**. This disparity might be attributed partly to the poor singlet energy transfer. However, a careful examination of the PLQY data reveals that the low quantum yield of **4Ac25CzPy** is mainly due to the relatively low $\Phi_{delayed}$ value, which is related to the triplet exciton characters. Since **4Ac25CzPy** has a higher T_1 energy of 2.96 eV, which is close to that of 3.1 eV for *o*-DiCbzBz, partial triplet excitons backflow from **4Ac25CzPy** to *o*-DiCbzBz becomes possible. This may explain why **4Ac25CzPy** has a relatively low PLQY in the doped film as well as the EL performance.

Besides, molecular orientation recently has been considered as a crucial factor in the molecular design of efficient OLED. To investigate the orientation of the transition dipole moment, angle dependent photoluminescence (ADPL) measurement for **4Ac25CzPy** and **4Ac35CzPy** incorporated with *o*-DiCbzBZ was conducted (Fig. S27, ESI†). A laser with an excitation wavelength of 325 nm is used to excite the mixed film, and the
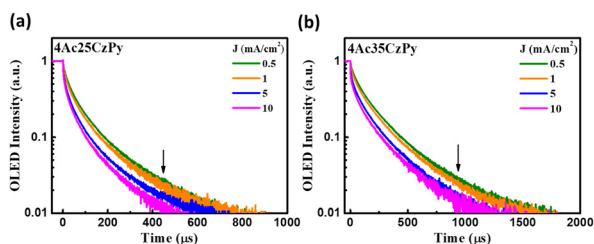

Fig. 9 TrEL signal with various current density (J = 0.5, 1, 5, 10 mA cm⁻²) for OLEDs employed (a) **4Ac25CzPy** and (b) **4Ac35CzPy**.

emissive intensity is monitored under different angles to probe the optical transition dipole and molecular alignment.[43] For comparison, two specifically ideal cases of molecules in perfectly horizontal orientation ($\Theta = 1$) and an isotropic orientation ($\Theta = 0.66$) are also performed, as shown in Fig. S27 (ESI†). The ADPL profiles for both two materials are found to align with the region isotropic orientation, resulting in the Θ_{ADPL} values of 0.62 and 0.63 for **4Ac25CzPy** and **4Ac35CzPy**, respectively. Even though our ADPL results indicates the absence of ordered alignment, the light out-coupling from the OLED is still very efficient and could achieve a high outcoupling efficiency (η_{EQE})[44] of 12.4% and 21.2% respectively. In short, the low efficiency of **4Ac25CzPy** device was attributed to the comprehensive effects that include lower PLQY in solid state, inefficient energy transfer from host to dopant, and less horizontal orientation relative to **4Ac35CzPy**, or perhaps having energy backflow to the host matrix due to its high triplet energy level.

Introduction of the carbazolyl moieties to the Ac–PM skeleton at various positions definitely creates certain extents of different perturbation to their conformational, electronic and photophysical behaviour. First, variation of their torsional angles can be clearly seen in the crystallographic analysis; while the conformation of the acridan in **4Ac35CzPy** is forced to be planar due to the steric repulsion of the carbazole groups on both sides, the torsional angle between the pyrimidine unit and the central phenyl ring is obviously smaller when compared with that of **4Ac25CzPy**, in which the steric hindrance arising from the adjacent carbazolyl group at the 2-position may favour to have the pyrimidine ring less conjugated with the phenylene unit. In addition, being squeezed in between two π-electron-rich carbazole groups at the 3,5-position, the acridan group in **4Ac35CzPy** shows a higher HOMO in the film state by 0.1 eV (Table 3), leading to a slightly red-shift of the CIE. Although both **4Ac25CzPy** and **4Ac35CzPy** demonstrate high PLQY in solution and have long luminescence decay time in the TrPL spectra, **4Ac35CzPy** exhibits minimal influence on its PLQY in the solid state, implying that the triplet quenching effects is small. This might be due to the intermolecular steric hindrance that suppresses the π–π stacking interactions and triplet excimer formation. Therefore, the triplet quenching effects are significantly reduced.

Conclusions

In summary, two novel AcPM based TADF emitters of **4Ac25CzPy** and **4Ac35CzPy** are successfully synthesized. They are recognized to exhibit pronounced TADF behaviour in the TrPL. As a result, OLEDs incorporating **4Ac25CzPy** and **4Ac35CzPy** achieve a maximum η_{EQE} of 12.4 and 21.2%, respectively. The EL performance of **4Ac35CzPy** and **4Ac25CzPy** OLED are comparable to acridan-pyrimidine-based TADF OLEDs reported in previous literatures.[14,45] The origin for the high efficiency in **4Ac35CzPy** has been investigated and found to be primarily attributed to the high PLQY value in solid state, which came from the well energy transfer from the host to the emitter, and high light out-coupling efficiency.

Author contributions

Ms Yi-Zhen Li and Mr Hsuan-Chi Liang were responsible for synthesizing the materials and analyzing their properties, Dr Chia-Hsun Chen and Mr Ching-Huang Chiu conducted the device fabrication and measurements, Prof. Jake A. Tan participated in the DFT calculation, Prof. Bo-Yen Lin and Ms Yi-Zhen Li collaborated on the result analysis and manuscript preparation, Prof. Man-kit Leung, Prof. Jiun-Haw Lee and Prof. Tien-Lung Chiu instructed the device design and measurement, and Prof. Man-kit Leung and Prof. Bo-Yen Lin also overseeing the paper writing and submission. All authors contributed to the discussion of the results for the manuscript preparation.

Conflicts of interest

There are no conflicts to declare.

Acknowledgements

Notes and references

1 H. Uoyama, K. Goushi, K. Shizu, H. Nomura and C. Adachi, *Nature*, 2012, **492**, 234–238.

2 Z. Yang, Z. Mao, Z. Xie, Y. Zhang, S. Liu, J. Zhao, J. Xu, Z. Chi and M. P. Aldred, *Chem. Soc. Rev.*, 2017, **46**, 915–1016.

3 Y. Im, M. Kim, Y. J. Cho, J.-A. Seo, K. S. Yook and J. Y. Lee, *Chem. Mater.*, 2017, **29**, 1946–1963.

4 Y. Liu, C. Li, Z. Ren, S. Yan and M. R. Bryce, *Nat. Rev. Mater.*, 2018, **3**, 1–20.

5 Y.-Z. Shi, H. Wu, K. Wang, J. Yu, X.-M. Ou and X.-H. Zhang, *Chem. Sci.*, 2022, **13**, 3625–3651.

6 Z. Cheng, Z. Li, Y. Xu, J. Liang, C. Lin, J. Wei and Y. Wang, *ACS Appl. Mater. Interfaces*, 2019, **11**, 28096–28105.

7 X. Liang, Z. L. Tu and Y. X. Zheng, *Chem. – Eur. J.*, 2019, **25**, 5623–5642.

8 R. Braveenth, H. Lee, S. Kim, K. Raagulan, S. Kim, J. H. Kwon and K. Y. Chai, *J. Mater. Chem. C*, 2019, **7**, 7672–7680.

9 L. Yu, Z. Wu, G. Xie, W. Zeng, D. Ma and C. Yang, *Chem. Sci.*, 2018, **9**, 1385–1391.

10 Q. Zhang, S. Sun, W. Liu, P. Leng, X. Lv, Y. Wang, H. Chen, S. Ye, S. Zhuang and L. Wang, *J. Mater. Chem. C*, 2019, **7**, 9487–9495.

14402 | *J. Mater. Chem. C*, 2023, **11**, 14395–14403

This journal is © The Royal Society of Chemistry 2023

11 T. Serevičius, R. Skaisgiris, I. Fiodorova, V. Steckis, J. Dodonova, D. Banevičius, K. Kazlauskas, S. Juršėnas and S. Tumkevičius, *Org. Electron.*, 2020, **82**, 105723.

12 Q. Zhang, S. Sun, W. J. Chung, S. J. Yoon, Y. Wang, R. Guo, S. Ye, J. Y. Lee and L. Wang, *J. Mater. Chem. C*, 2019, **7**, 12248–12255.

13 R. Komatsu, H. Sasabe and J. Kido, *J. Photonics Energy*, 2018, **8**, 032108.

14 I. S. Park, H. Komiyama and T. Yasuda, *Chem. Sci.*, 2017, **8**, 953–960.

15 K. Nakao, H. Sasabe, R. Komatsu, Y. Hayasaka, T. Ohsawa and J. Kido, *Adv. Opt. Mater.*, 2017, **5**, 1600843.

16 I. S. Park, J. Lee and T. Yasuda, *J. Mater. Chem. C*, 2016, **4**, 7911–7916.

17 K. C. Pan, S. W. Li, Y. Y. Ho, Y. J. Shiu, W. L. Tsai, M. Jiao, W. K. Lee, C. C. Wu, C. L. Chung and T. Chatterjee, *Adv. Funct. Mater.*, 2016, **26**, 7560–7571.

18 K. Wu, T. Zhang, L. Zhan, C. Zhong, S. Gong, N. Jiang, Z. H. Lu and C. Yang, *Chem. – Eur. J.*, 2016, **22**, 10860–10866.

19 P. Ganesan, R. Ranganathan, Y. Chi, X. K. Liu, C. S. Lee, S. H. Liu, G. H. Lee, T. C. Lin, Y. T. Chen and P. T. Chou, *Chem. – Eur. J.*, 2017, **23**, 2858–2866.

20 R. Komatsu, H. Sasabe, Y. Seino, K. Nakao and J. Kido, *J. Mater. Chem. C*, 2016, **4**, 2274–2278.

21 Y.-T. Lee, P.-C. Tseng, T. Komino, M. Mamada, R. J. Ortiz, M.-K. Leung, T.-L. Chiu, C.-F. Lin, J.-H. Lee and C. Adachi, *ACS Appl. Mater. Interfaces*, 2018, **10**, 43842–43849.

22 V. Myrseth, J. Bozek, E. Kukk, L. Sæthre and T. Thomas, *J. Electron Spectrosc. Relat. Phenom.*, 2002, **122**, 57–63.

23 P. J. Stephens, F. J. Devlin, C. F. Chabalowski and M. J. Frisch, *J. Phys. Chem.*, 1994, **98**, 11623–11627.

24 C. Lee, W. Yang and R. G. Parr, *Phys. Rev. B: Condens. Matter Mater. Phys.*, 1988, **37**, 785.

25 A. Becke, 1993.

26 F. Neese, F. Wennmohs, A. Hansen and U. Becker, *Chem. Phys.*, 2009, **356**, 98–109.

27 S. Grimme, S. Ehrlich and L. Goerigk, *J. Comput. Chem.*, 2011, **32**, 1456–1465.

28 V. Barone and M. Cossi, *J. Phys. Chem. A*, 1998, **102**, 1995–2001.

29 F. Neese, F. Wennmohs, U. Becker and C. Riplinger, *J. Chem. Phys.*, 2020, **152**, 224108.

30 F. Neese, *Wiley Interdiscip. Rev.: Comput. Mol. Sci.*, 2022, **12**, e1606.

31 F. Neese, *J. Comput. Chem.*, 2023, **44**, 381–396.

32 T. Lu and F. Chen, *J. Comput. Chem.*, 2012, **33**, 580–592.

33 Q. Zhu, X. Guo and J. Zhang, *J. Comput. Chem.*, 2019, **40**, 1578–1585.

34 X.-K. Chen, D. Kim and J.-L. Brédas, *Acc. Chem. Res.*, 2018, **51**, 2215–2224.

35 P. K. Samanta, D. Kim, V. Coropceanu and J.-L. Brédas, *J. Am. Chem. Soc.*, 2017, **139**, 4042–4051.

36 J.-J. Huang, Y.-H. Hung, P.-L. Ting, Y.-N. Tsai, H.-J. Gao, T.-L. Chiu, J.-H. Lee, C.-L. Chen, P.-T. Chou and M.-K. Leung, *Org. Lett.*, 2016, **18**, 672–675.

37 K. Masui, H. Nakanotani and C. Adachi, *Org. Electron.*, 2013, **14**, 2721–2726.

38 H. Lim, H. J. Cheon, S. J. Woo, S. K. Kwon, Y. H. Kim and J. J. Kim, *Adv. Mater.*, 2020, **32**, 2004083.

39 B.-Y. Lin, T.-C. Lin, T.-L. Chiu, J.-H. Lin, C.-H. Chen, J.-H. Lee and M.-K. Wei, *Org. Electron.*, 2021, **96**, 106237.

40 S. Reineke, T. C. Rosenow, B. Lüssem and K. Leo, *Adv. Mater.*, 2010, **22**, 3189–3193.

41 J. Grüne, N. Bunzmann, M. Meinecke, V. Dyakonov and A. Sperlich, *J. Phys. Chem. C*, 2020, **124**, 25667–25674.

42 S. Hu, J. Zeng, X. Zhu, J. Guo, S. Chen, Z. Zhao and B. Z. Tang, *ACS Appl. Mater. Interfaces*, 2019, **11**, 27134–27144.

43 T. Morgenstern, M. Schmid, A. Hofmann, M. Bierling, L. Jäger and W. Brütting, *ACS Appl. Mater. Interfaces*, 2018, **10**, 31541–31551.

44 P.-Y. Chou, H.-H. Chou, Y.-H. Chen, T.-H. Su, C.-Y. Liao, H.-W. Lin, W.-C. Lin, H.-Y. Yen, I.-C. Chen and C.-H. Cheng, *Chem. Commun.*, 2014, **50**, 6869–6871.

45 R. Komatsu, T. Ohsawa, H. Sasabe, K. Nakao, Y. Hayasaka and J. Kido, *ACS Appl. Mater. Interfaces*, 2017, **9**, 4742–4749.

This journal is © The Royal Society of Chemistry 2023

J. Mater. Chem. C, 2023, **11**, 14395–14403 | **14403**